Review Paper:

A brief overview of X-ray photoelectron spectroscopy characterization of thin films

Ho Soonmin[1]* and Jacob A.G.[2]
1. Faculty of Health and Life Sciences, INTI International University, Putra Nilai,71800, Negeri Sembilan, MALAYSIA
2. Department of Chemistry, Enzyme Technology and Green Synthesis Group Biotechnology and Biochemistry Laboratory, Level 1, T05, Faculty of Science, NIGERIA
*soonmin.ho@newinti.edu.my

Abstract

Preparation and characterization of nanostructured thin films have been reported by many researchers. X-ray photoelectron spectroscopy (XPS) method has been used over few decades in different fields such as superconductor, semiconductor, metallurgy and catalysis. In this work, elemental oxidation state, electronic state, chemical structure and chemical composition were investigated for metal sulfide, metal selenide, metal oxide and metal telluride films.

Evaluation of binding energy for the obtained samples was reported. XPS spectra showed that annealing treatment has a very strong effect on the composition of the films. The elemental oxidation state and electronic state were strongly dependent on the specific experimental conditions.

Keywords: X-ray photoelectron spectroscopy, thin films, semiconductor, band energies, elemental composition.

Introduction

The chalcogenide material could be used in light emitting diodes, solar cells[32], opto electronic device, thin film transistors, optical window, laser screens and sensor devices. Nanostructured thin films have been synthesized using various deposition methods[33]. During the deposition process, annealing[31] and doping were employed to enhance the conductivity value.

The properties and characterization of prepared metal sulfide[113], metal telluride, metal oxide and metal selenide films have been studied using different tools. Atomic force microscopy[73,87] and Scanning electron microscopy[30] were used to investigate the morphology of films. X-ray diffraction[62] and energy dispersive X-ray analysis[68] were employed to study the structure and composition of samples. Photoluminescence spectrum[3] and Fourier transform infrared spectroscopy[41] were utilized to determine the electronic structure and functional group of film. UV-spectrophotometer could be used to measure the band gap[76], absorption and transmittance value[81].

X-ray photoelectron spectroscopy (XPS) is used to determine the quantitative elemental composition and oxidation state of materials, stoichiometry, electrical state and examine surface contamination. On a broader spectrum, XPS is applicable for characterizing the surfaces of semiconductors, inorganic minerals, organic compounds, thin films and coated materials[19]. Both XPS and energy-dispersive x-ray spectroscopy (EDS) are used to detect the presence of elements in different materials[38]. However, the former technique provides information on the elemental composition of materials and differentiates the oxidation states of the elements[61], by taking measurements within a few atomic layers usually from the top 1–10 nm on the surface, the latter method can determine the bulk composition of the elements with excitation volumes as deep as 3 µm deep into the sample[55].

As a surface analytical technique[37], XPS can solve some problems such as what elements are there on the surface of a solid material and what states are the elements at the surface? Interestingly, this technique can be applied to investigate depth-profiling of thin films[5] by ion sputtering while quantifying the matrix-level elements as a function of depth. XPS is a unique elemental analysis method which can provide information on the chemical state of the detected elements[16] (differentiating between the sulphate and sulphide forms of elemental sulphur). It is a proven electron spectroscopic tool for studying sputter depth-profiling of films to examine material changes in layer structures[53]. Some sputtering profiling can probe hundreds of nanometers to micrometers into a material which may take some hours to complete. Generally, argon ion has been the most widely available sputtering source.

XPS was applied by Oswald and co-workers[75] to investigate a Ti/Al thin film covered with aluminium nitride barriers at high temperatures. The peak fitting component of XPS allowed separation of the Ti and N signals. The workers observed that aluminium nitride barriers were stable until 600 °C while the Al was partial preferential oxidized.

XPS was used to determine the chemical composition of catalyst supports and enzyme-based catalysts at their molecular echelons to identify various elements excluding hydrogen and helium[89] with detection limits of about 0.1%–1%.

Therefore, it is pertinent to note that with this spectroscopic method, vital information on the effectiveness of a newly prepared films can be generated[92] and being a reliable and informative analytical method for providing a qualitative information can be interpreted effortlessly. Most often, XPS is used to acquire information on chemical composition,

adsorbates, surface functionalization, layer thickness and on few occasions, particle size of nanomaterials can be determined.

Principle of X-ray photoelectron spectroscopy

XPS works on the fundamental of x-rays knocking off electrons from the surface of a material. The energy of these electrons, which is associated with the nature and strength of their chemical bonds, is determined to measure the composition of the material under investigation[49]. Only the electrons formed at the surface of the sample can escape and could be detected[59]. This process operates by irradiating a sample with monochromatic X-ray radiation, which results in emission of some photoelectrons having the energies that are characteristic of the elements inside the sampling volume[109].

XPS application is centered on Einstein's photoelectric effect wherein electrons are ejected from atoms due to impact of electromagnetic radiation[92]. In this process, photoelectrons are emitted from a sample once the energy of the impacting photons surpasses the binding energy of the electrons in the sample. Considering that XPS operates[64] in the energy ranges between 50 and 1200 eV, the values of the wavelength (λ) are usually very small, which only correspond to a limited monolayer. For photoelectrons to be effectively detected, they need to emanate from atomic layers close to the surface.

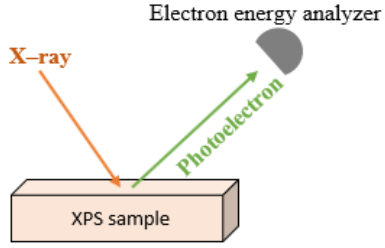

Figure 1: Fundamental illustration of XPS technique

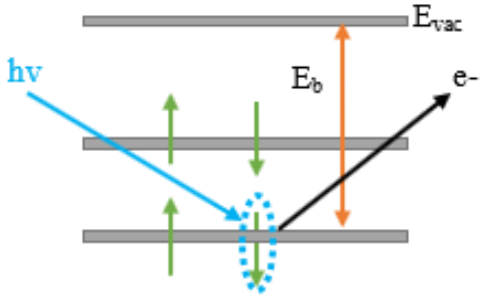

$E_k = hv - E_b - \varphi_{sp}$
E_k = kinetic energy
E_b = binding energy
h = Planck's constant
v = frequency of X-rays
φ_{sp} = spectrometer work function

Figure 2: Energy equation and principle of XPS

As a result, electron spectroscopy is highly surface-specific. The kinetic energy of an emitted electron corresponds to its binding energy[45] and since all atoms possess manifold orbitals at different energy levels, the resultant emitted electrons exist in ranges with different binding energies thus creating an XPS spectrum[29]. Figure 1 depicts a simple diagram explaining the fundamental principle of XPS for surface analysis.

The spectrum was produced by plotting the binding energy (X-axis) against the number of electrons formed (Y-axis). Spectra are either conveyed in survey mode which depicts inventories of elements on a sample surface, or high-resolution scans for relevant peaks to detect the chemical bonds in the elements under investigation[86]. Subsequently, the binding energies of several photoelectrons emanating from a sample surface are used as evidence to identify elements present on the surface. The core electrons (with kinetic energy E_k) were emitted by the incident X-rays as highlighted in figure 2.

When the element entered a different oxidation state, the binding energy was changed, leading to the chemical moving in spectrum[15]. In other words, elevated oxidation state increases the binding energy. The various photoelectron peaks in a spectrum represent distinct binding energies of the electrons existing in the sample could be observed.

Advantages and Disadvantages of XPS

XPS is a well-known surface analysis method and it was used by many researchers[20]. Major advantages of this spectroscopy include surface sensitivity (~10 nm) and the capacity to differentiate variations in chemical environment. XPS is a quantitative and relatively non-destructive technique without standard[37]. Charge neutralizers are used to resolve the problem associated with charging insulation samples. Considering that XPS is highly surface sensitive, caution is taken to prevent surface contamination.

There are limitations of XPS which are not associated with samples and their preparations, but on the instrumentation. XPS cannot detect hydrogen and helium, which results to a ratio of elements in a material that may not be completely accurate (since there always exists some amount of hydrogen in many samples). Thus, it is a common error to believe that the percentage of atoms found in XPS experiments are entirely correct owing to the undetected hydrogen. One approach to detect hydrogen by XPS is to wash the sample with sodium naphthalenide, replacing hydrogen with sodium. Nevertheless, the result may be inaccurate and time-consuming.

The electrons residing in the lower depth of a sample lose some energy as they meet other atoms whereas the surface electrons retain their initial kinetic energy. Therefore, XPS data is only based on average measurement. Furthermore, the electrons in the lower region are susceptible to elastic scattering which may have a significant effect on the result at higher angles of emission. Also, because the X-ray beam

is comparatively wide having the minimum width range of 10–200 μm, (only give average composition in the beam area), XPS is incapable of distinguishing sections of elements which are smaller compared to the size of the beam.

XPS studies of metal oxide films

The p-type copper oxide films could be used as photo electrode (green energy carrier) for solar water splitting applications. Sol gel spin coating method and electrodeposition technique were used to prepare CuO films (substrate=ITO glass, precursor=copper acetate, rotation speed=2000 rpm, duration=30 seconds) and Cu_2O films (substrate=FTO glass, precursor=copper sulfate, temperature=room temperature, counter electrode=platinum wire; reference electrode=silver/silver chloride) respectively[13]. The peaks at 529.7 eV and 530.3 eV were contributed to lattice oxygen in the CuO and Cu_2O respectively.

Also, XPS analysis (figure 3) revealed several peaks attributed to Cu $2p_{3/2}$ and Cu $2p_{1/2}$ in CuO (933.3 eV and 953.6 eV) and Cu_2O (932.8 eV and 952.5 eV). The band gap was 2.45 eV in Cu_2O films while different band gap values could be observed in the as-deposited CuO (1.49 eV), annealed (300 °C) films (1.61 eV) and annealed (400 °C) films (1.51 eV). Based on the PEC water splitting experiments, annealed sample (at 300 °C=efficiency was 0.45% and 400 °C=efficiency was 1.19%) showed better performance than the as-deposited CuO (efficiency was 1.05%) and Cu_2O films (efficiency was 0.09%).

Quaternary compounds such as CuSnSO films were grown on indium tin oxide (ITO) glass using copper sulphate, tin sulphate and sodium thiosulfate in the acidic solution via electro chemical deposition method[115]. The platinum sheet and saturated calomel electrode (SCE) were used as counter electrode and reference electrode respectively. The photovoltaic behaviors included fill factor (0.3), power conversion efficiency ($4.9x10^{-3}$%), short circuit current density (0.1 mA/cm^2) and open circuit voltage (0.165 V).

Poor photovoltaic properties were due to the cell structure and poor crystallinity. The band offset of the prepared films (concentration of tin sulphate=3mM, deposition potential=-0.8 V, film thickness=0.5 μm) was studied using XPS method (figure 4). The energy separation between valence band maximum and tin (Sn) 4d core level for CTSO was 25.25 eV. Meanwhile, separation between valence band maximum and the zinc 3d core level for zinc oxide was 8.1 eV.

The aluminium-doped zinc oxide films have been produced[79] via atomic layer deposition method (substrate = glass, temperature = 80 °C, precursor = trimethylaluminium, deionized water, diethylzinc, carrier = nitrogen gas, flow rate=600 sccm). These materials could be used in optoelectronic and display devices due to high conductivity value, high transparency, excellent thermal stability and mechanical flexibility. Based on the XPS results, the Zn $2p_{3/2}$ peaks were observed at 2.23 eV and 2.18 eV for as-deposited films and annealed samples (30 minutes, 600 °C) respectively. The O1s peaks of annealed films and as-deposited films were observed to be 531.3 eV and 532.3 eV respectively, indicating O^{2-} ions bonded to the zinc ions (in the wurtzite phase). It was noted that annealed sample has lower amount of oxygen (O_2) vacancies.

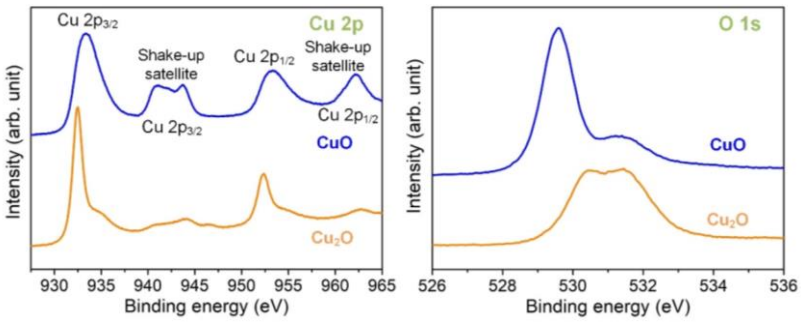

Figure 3: XPS spectra of Cu 2p and O 1s for Cu_2O films and CuO films[13]

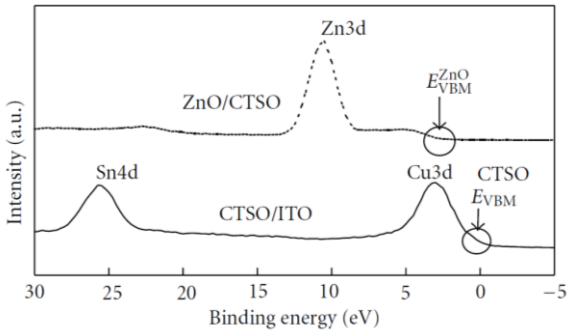

Figure 4: XPS analysis[115] for the zinc oxide and $Cu_{1.7}Sn_{0.084}S_{0.13}O$

The p-type $CuCrO_2$ film has acceptable thermal stability and low deposition temperature[2]. The resistivity was 0.66 ohm and the transmittance value about 60%. The radio frequency magnetron sputtering deposition technique has been used to produce thin films (substrate= quartz, RF power (Cr_2O_3)=200W, RF power (Cu_2O)=50W, sputtering gas=argon, base pressure=$5x10^{-7}$ Torr, substrate temperature=400 °C, sputtering gas flow rate=10 sccm, film thickness=125 nm). The peak position, full-width half maximum (FWHM) and oxidation state were described based on the XPS data (Table 1).

It was noted that all the grains could undergo coalescence when the thermal energy was increased. The average grain size increased (40.22 nm to 105.3 nm) when the annealing temperature was increased from 600 °C to 900 °C. The heterojunction studies were performed using n-ITO films (400 nm thick) and $CuCrO_2$ sample (200 nm). The best experimental findings including cut-in voltage (0.85V), low leakage current ($1.24x10^{-8}$ A/cm^2), ideality factor (value=4.13) and rectification ratio (value=2375) were highlighted. Hafnium (Hf) oxide films have been produced using plasma enhanced atomic layer deposition method[17]. This method shows some advantages such as reduced the deposition temperature, increased the growth rate and could select precursors if compared to atomic layer deposition technique. Experimental results showed that bigger surface density and higher surface roughness could be observed when the growth per cycle and oxygen plasma time were increased. The composition of the obtained samples (prepared under different conditions) was studied [Table 2]. All the films indicated slightly rich in oxygen due to native SiO_2 layer. Also, the XPS data confirmed Hf-O bonding signals with small amount of impurity such as carbon (less than 4.25%) and nitrogen (5.75%).

Ga_2O_3 films with 6-15 nm grain size and surface area greater than 100 m^2/g could be prepared via flame spray pyrolysis method[101]. These n-type semiconductors were used in gas sensor applications (reducing gas and oxidizing gas). Based on the XPS results (figure 5), the Nb content increased (3.9 % to 8.7 %) when the annealing temperature was increased from 500 °C to 900 °C, because of migration of niobium (V) ions into crystal surface ($GaNbO_4$ phase). XRD data highlighted that particle radius was smaller than 3 nm if the annealing temperature below 800 °C.

The highest grain size was 19 nm when the films was synthesized at 1000 °C. The chemical state of gallium (Ga) was investigated for the films prepared at various conditions (0,1,2 and 4=0,1,2 and 4 mol % of Nb (V) cation) also. The ratio (in XPS peak areas) of Ga (I) to Ga (III) was one to eight, indicating the transformation occurred without additional free charge carriers.

Table 1
The FWHM, peak position and oxidation peak for the $CuCrO_2$ films[2] produced at 650 °C

Peak	Oxidation state	Binding energy (eV)	FWHM (eV)
Cu $2p_{3/2}$	Cu^{+1}	932.27	3.52
Cu $2p_{1/2}$	Cu^{+1}	952.4	1.56
Cr $2p_{3/2}$	Cr^{3+}	576.16	4.45
Cr $2p_{1/2}$	Cr^{3+}	586	3.43

Table 2
The atomic concentrations of carbon, oxygen, hafnium and nitrogen in the HfO_2 films prepared at various oxygen flow rates and oxygen plasma power[17]

	Conditions			
Atomic Concentrations (at %)	**10 sccm and 20 W**	**10 sccm and 300W**	**50 sccm and 20 W**	**50 sccm and 300W**
C 1s	2.53	2.31	4.25	4.12
N 1s	4.86	4.64	5.75	5.66
O 1s	65.53	65.90	63.38	63.22
Hf 4f	27.08	27.15	26.62	26.99
Atomic ratio				
Hf:O	1:2.42	1:2.43	1:2.38	1:2.34

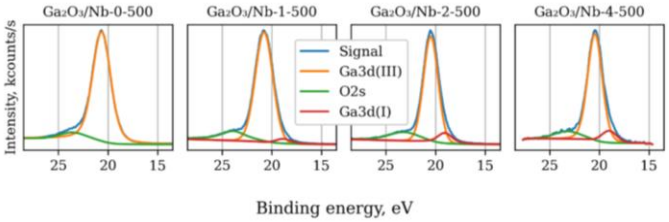

Figure 5: Deconvolution[101] of Ga3d XPS spectra of the obtained films with various niobium content (at 500 °C).

Based on the literature survey, the properties of TiO_2, CdO, cerium-doped CdO, PbO, MgO, FeO, Fe_2O_3, NiO, SnO, Au-Al_2O_3 and Re-Al_2O_3 have been studied using XPS technique. The compositional, phase structure and surface chemistry were reported as indicated in table 3.

XPS studies of metal telluride films: Zinc telluride could be used as stable back contact in the heterojunction solar cells. These p-type conduction materials show low resistance, high absorption coefficient (10^5 cm^{-1}) and can absorb visible light easily. The close spaced sublimation method[108] has been employed for the preparation of zinc telluride films (substrate=glass slide, distance between source and substrate=5mm, heat source=halogen lamps of 1000 Watts). The XPS measurements were conducted (figure 6), the oxidation states of Cu^{+1}, Te^{2+} and Zn^{2+} could be observed. Several peaks for Zn $2p_{3/2}$ (1024.48 eV-Zn^{2+} oxidation, 1023.63 eV-zinc metallic) and Zn $2p_{1/2}$ (1048.3 eV-Zn^{2+} oxidation, 1046.84 eV-zinc metallic) could be found in un-doped ZnTe films. Meanwhile, numerous peaks for Zn $2p_{3/2}$ (1030.49eV) and Zn $2p_{1/2}$ (1053.61eV) were observed in Cu-doped ZnTe films.

Table 3
XPS results for the different types of metal oxide thin films

Thin films	XPS highlighted results
Re-Al_2O_3	• High-loaded catalyst consisted of 94.5% of rhenium (Re), however, low-loaded catalyst contained 60.5%. • Oxidation at 300 °C observed the formation of Re_2O_7 while, at 150 °C enhanced the production of Re^{4+}-Re^{7+} species[74].
Au-Al_2O_3	• In the as-deposited samples, the O1s peak has been shifted to lower binding energy, while the Al 2p peak has been moved to higher energy (due to the incorporation of the Au particles). • Au-Al_2O_3 films have been deposited onto quartz using rf co-sputtering method[27].
SnO	• The binding energies of the core lines of the tin (Sn $3d_{5/2}$=487 eV-486.8 eV) and oxygen (O1s=530.7 eV to 533.2 eV) did not change when the annealing temperature was increased (450 °C to 650 °C). • In the palladium-doped films, Pd $3d_{5/2}$, Sn $3d_{5/2}$ and O 1s showed binding energy of 335.9eV-338.9 eV, 487.2 eV and 531 eV-533.7 eV, respectively[24].
SnO	• The main O1s and Sn $3d_{5/2}$ lines could be observed at 530.5 eV and 486.7 eV, respectively in as-deposited tin oxide films[65] • In the annealed films, different platinum chemical states could be seen in the air-treated films (platinum (IV) ions=74.6 eV for Pt $4f_{7/2}$) and carbon dioxide/argon treated samples (platinum (II) ions=72.7eV for Pt $4f_{7/2}$).
NiO	• Deconvolution[77] of XPS data highlighted that atomic percentage for Ni 2pNi^{2+}, Ni 2pNi^{3+} and O1s have varied with variation in oxygen flow rate (5, 8 and 10 sccm). • There are different bonding energies can be seen in Ni 2p Ni^{3+} (857.21 eV to 872.86 eV), Ni 2p Ni^{2+} (853.58 eV to 879.02 eV) and O1s (529.16 eV to 533.26 eV).
FeO, Fe_2O_3	• The peaks were recorded at 723.3 eV & 707.9 eV and 724.3 eV & 711 eV for the Fe $2p_{1/2}$ and Fe $2p_{3/2}$, respectively in FeO and Fe_2O_3 samples[26]. • XPS data confirmed that hematite (α-Fe_2O_3 was hexagonal phase) and maghemite (γ-Fe_2O_3 was cubic phase) have almost identical results. Additionally, difference phases could be observed (in the lattice structure), did not result in significant chemical shifts.
MgO	• It was noticed that binding energy of O2s and O2p was moved to lower state after the etching process[96]. • The etched samples showed two peaks (MgO and $Mg(OH)_2$) while hydrated films indicated only one peak ($Mg(OH)_2$).
PbO	• The contribution of Pb $4f_{7/2}$ and Pb $4f_{5/2}$ with binding energies of 137.7 eV and 142.6 eV, indicating PbO_2 films[42]. • It was noted that 529.1 eV and 530.8 eV corresponding to the O 1s.
TiO_2	• The Ti°(453-454 eV), Ti^{2+}(455.1 eV), Ti^{3+} (457.8 eV) and Ti^{4+} (458.7 eV) could be observed in the Ti $2p_{3/2}$ spectra when the XPS was investigated at 6nm depth from the surface of the films[78]. • The influence of different oxygen flow rates such as 15 sccm (Ti^{2+} and Ti°), 17.5 sccm (Ti^{2+} was dominant structure), 20 sccm (Ti^{4+}), was reported.
CdO, cerium (Ce)-doped CdO	• The presence of O^{2-} (530 eV=O1s) and Cd^{2+} (Cd $3d_{5/2}$) could be confirmed from the obtained binding energies[103]. • Several peaks such as Cd 3 $d_{5/2}$ (406eV), Cd $3d_{3/2}$ (411 eV), Cd $3p_{3/2}$ (618 eV), Cd $3p_{1/2}$(652 eV), Ce $3d_{5/2}$(882.7 eV) and O1s (530 eV) were obtained in the XPS spectra.

On the other hand, de-convoluted Te $3d_{5/2}$ and Te $3d_{3/2}$ peaks could be seen at 587.46 eV and 576.96 eV (in in-doped films) and 586.96eV and 576.86 eV in Cu-doped films respectively. The resistivity dropped (from 10^6 to 1 Ωcm) after Cu doping because of increase in charge carriers in zinc telluride films. Following that, the unit cell volume increased and eventually reduction of band gap could be seen.

The p-type antimony telluride (Sb_2Te_3) films could be used in solar cells, thermoelectric generators and coolers due to low band gap, low thermal conductivity, long-term stability and high Seebeck co-efficient. These V-VI group materials have been produced at room temperature[7] using vacuum co-evaporation method (sources=Sb foil and Te powder, substrate=glass, pressure=$9x10^{-4}$ Pa).

This deposition method has some advantages such as short fabrication time, simple equipment and desirable stoichiometry films. Annealed films (at 613K) could reduce the grain boundary density, promote the formation of Sb-Te bond and prevent oxidation of sample's surface. Bigger grain and higher root mean square (7.6 nm) could be found in the annealed films than as-deposited films. Other results such as mobility (169.86 $cm^2/V.S$), Hall co-efficient (0.11 cm^3/C) and carrier concentration ($5.87x10^{19}$ cm^{-3}) were reported in annealed samples. In the XPS data, some peaks at 572.5 eV and 582.9 eV for Te $3d_{5/2}$ and Te $3d_{3/2}$ were observed respectively. Meanwhile, the values of 530.3 eV ($3d_{5/2}$) and 539.6 eV ($3d_{3/2}$) were attributed to Sb-O bonding, 538-539 eV ($3d_{3/2}$) and 529-530 eV ($3d_{5/2}$) were contributed to Sb metallic bonding. Finally, the Sb-Te bond was described at 528.9 eV and 538.2 eV. The antimony telluride could be utilized as buffer layer (increase the conductivity and produced tunneling barrier) between metal electrode and absorber layer in the solar cells.

According to the literature survey, the properties of $Bi_2(Te_{0.5}Se_{0.5})_3$, Eu-doped Bi_2Te_3, Cs_2Te, GdZnTe, SnTe, CuTe, Cu_2Te, $Cu_{0.5}Te$, HgTe, PbGeTe, $MoTe_2$, WTe_2, $PtTe_2$, Cr_2Te_3, GaTe, Bi_2Te_3, CdTe and CdZnTe films have been studied using XPS technique. The compositional, phase structure and surface chemistry are reported as indicated in table 4.

XPS studies of metal selenide films: Cadmium selenide films have grown on (100) n-doped silicon substrate[107] at room temperature in the sulfuric acid solution (deposition cycles=30 cycles, deposition potential=-0.8V versus Ag/AgCl, reference electrode= silver/silver chloride, precursors= cadmium sulphate and sodium selenite (Na_2SeO_3)). The prepared films exhibited better coverage of the surface, smaller grains and cubic zincblende structure. XPS investigations (figure 7) showed several peaks compatible with Se^{2-} ion (54 eV to 54.3 eV) and Cd^{2+} ion (404.9 eV to 406 eV).

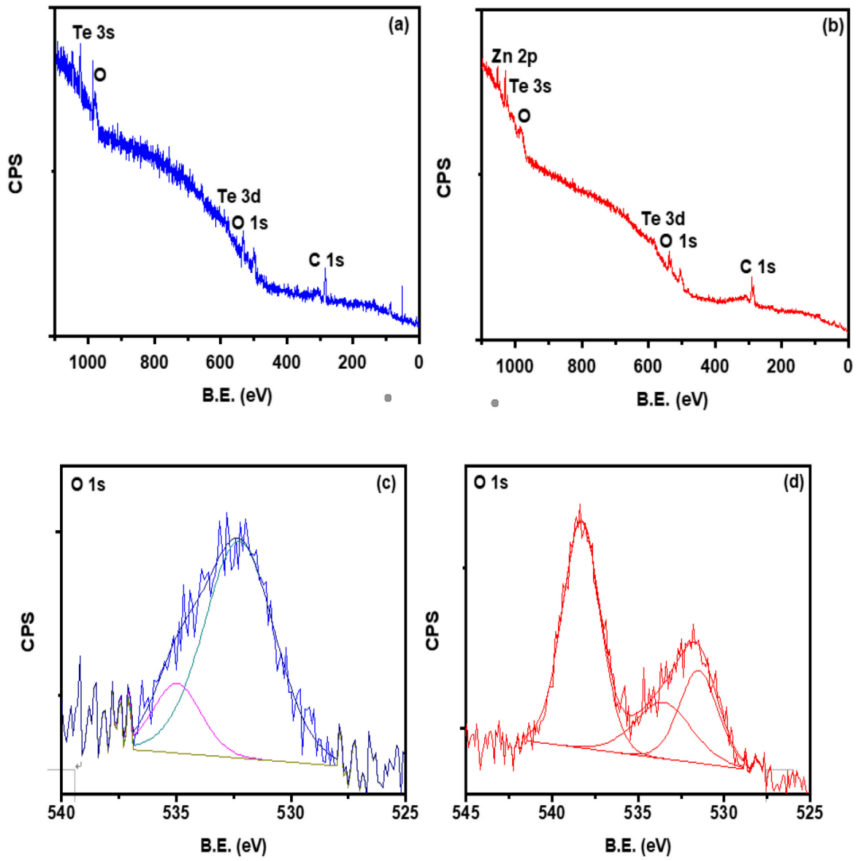

Figure 6: XPS Survey scan of (a) un-doped and (b) Cu-doped zinc telluride films. De-convoluted XPS analysis of Oxygen-1s for (c) un-doped and (d) Cu-doped zinc telluride films[108].

Table 4
XPS results for the different types of metal telluride thin films.

Thin films	Highlighted XPS results
$Bi_2(Te_{0.5}Se_{0.5})_3$	• Atomic percentage of Bi, Te and Se were reported to be 42.07%, 28.13% and 27.52%, respectively. • Binding energies of 596.5 eV (Te), 175.5 eV (Bi) and 54.5 eV (Se) could be detected[58].
Eu-doped Bi_2Te_3	• XPS data[12] confirmed europium (Eu) entered Bi_2Te_3 matrix in the divalent state (Eu^{2+}).
Cs_2Te	• Binding energies of 571.6 eV (Te^{-2} $3d_{5/2}$) and 581.9eV (Te^{-2} $3d_{3/2}$) could be detected[54]. • The Cs 3d could be observed about 165 eV in the obtained cesium telluride films
GdZnTe	• The peaks of Te $3d_{5/2,3/2}$ (572.4eV-586.3eV), Zn $2p_{3/2,1/2}$ (1021.3 eV-1045.1eV) and Gd $3d_{5/2,3/2}$ (1186.8eV-1218.6eV) could be detected in gadolinium-zinc-telluride films[22].
CuTe, Cu_2Te, $Cu_{0.5}Te$	• The $Cu_{0.5}Te$ films showed 87.33% of Te^{2-} and 12.66% of Te°. • The CuTe indicated 76.64% of Te^{2-}, 16.84% of Te° and 6.52% of Te^{4+}. • Cu_2Te films[43] exhibited 41.7% of Te^{2-}, 11.54% of Te° and 46.76% of Te^{4+}.
CuTe	• The atomic percentage of copper dropped (62.87% to 58.54%) but tellurium increased (9.48% to 11.65%) when the concentration of potassium telluro-pentathionate ($K_2TeS_4O_6$) was increased (0.025 M to 0.1 M). • The copper:sulphur:tellurium ratio reduced when the duration of chalcogenization was increased[36].
HgTe	• ΔE Hg $5d_{5/2}$ and ΔE Hg $5d_{3/2}$ were 0.88eV and 0.83 eV, respectively. • It was noted that Te $4d_{5/2}$ (40.8eV) with binding energy move of 1.12eV from bulk value[82].
PbGeTe	• The peaks[111] of Ge $2p_{3/2}$, Te $3d_{5/2}$ and Pb $4f_{7/2}$ are at binding energies 1217.6 eV, 571.5 eV and 137.7 eV, respectively. • Intensity ratio of Pb:Te was 0.5. • The intensity ratio of Ge:Te was 0.11.
$MoTe_2$, WTe_2, $PtTe_2$	• The peaks of Mo 3d and Te 3d are at binding energies 224 eV-240 eV and 568eV-591eV, respectively. • The peaks of W 4f and Te 3d are at binding energies 30eV-48eV and 569eV-591eV, respectively[18]. • The peaks of Pt 4f and Te 3d are at binding energies 68eV-82eV and 569eV-591eV, respectively.
GeTe	• The peaks of Ge $2p_{3/2}$, Ge 3d, Te $3d_{5/2}$ and Te $3d_{3/2}$ are at binding energies 1217.5eV, 29.4eV, 571.8eV and 583.1 eV respectively[91].
Bi_2Te_3	• The peaks of Te^{2+} 3d and Te^{4+} 3d are at binding energies 571.3eV-581.6 eV and 572 eV- 582.3 eV, respectively[50]. • The peaks of Bi^{3+} 4f and Bi^{5+} 4f are at binding energies 155.6 eV -160.9 eV and 156.1 eV-161.4eV, respectively.
WTe_2	• The peaks of W^{4+} $4f^{7/2}$ and W^{4+} $4f^{5/2}$ are at binding energies 31.7eV and 33.7 eV, respectively[116]. • Binding energies of 583.6 eV (Te^{2-} $3d_{3/2}$), 572.6 eV (Te^{2-} $3d_{5/2}$) could be detected.
CuTe	• The peak of Te 3d5 is at binding energy 575.5 eV, indicated Te^{2-} ion. • The Cu 3p indicated Cu^{+} ion[99].
CdTe	• Atomic concentration[106] of tellurium reduced (14% to 5.8%) when the films were prepared on titanium nitride substrate at more negative potential (from -0.4 V to -0.65 V versus Ag/AgCl). • Nearly equal amounts of cadmium (7.4%) and tellurium (7.2%) when the films were synthesized on molybdenum substrate at deposition potential of -0.45 V
Bi_2Te_3	• The peaks of Bi $4f_{7/2}$ and Bi $4f_{5/2}$ are at binding energies 158 eV and 163 eV, respectively[52]. • The binding energies of the Te $3d_{5/2}$ and Te $3d_{3/2}$ are located at 572 eV and 582.2 eV, respectively.
czt	• CdZnTe (CZT) films have been chemically etched via bromine in methanol treatment. The obtained films showed tellurium rich surface layer. • The concentration of tellurium (66%), cadmium (28%) and zinc (6%) were measured[88].
CdTe, CdZnTe (CZT)	• Cd $3d_{5/2}$ was observed at 403.2 eV (CdTe) and 405.1 eV (CZT). • Cd $3d_{3/2}$ was detected at 410 eV (Cdte) and 411.9 eV (CZT). • Te $3d_{3/2}$ was seen at 573.1 eV (CdTe) and 577 eV (CZT). • Te $3d_{5/2}$ was found[70] at 583.6 eV, 587.3 eV (CdTe) and 582.1eV, 585.7 eV (CZT).
Cr_2Te_3	• There are 2 peaks could be detected in Cr 3s, indicating the itinerant nature of this films[98]. • The ratio of Cr 2p and Te 3d was 2.67.
GaTe	• GaTe films[44] processed in deoxygenated solvents showed Ga 3d (19.5 eV), Te $3d_{3/2}$ (583.5eV) and Te $3d_{5/2}$ peaks (572.9 eV).

CdTe	• In the cadmium chloride treatment, chlorine penetrated into CdTe layer (during the annealing process). The chlorine concentration was about 0.15% in the obtained films[1].
SnTe	• Te $3d_{5/2}$ peak close to Te^{4+} and Te. • During the oxidation process[71], additional components have been moved to higher binding energies (1.1 eV) in Sn 3d.
CdTe	• The percentage atomic concentration of cadmium and tellurium were 26.5% and 25.9%, respectively in as-deposited films[14]. • The percentage atomic concentration of cadmium and tellurium were 12.4% and 21.3%, respectively in treated samples (leaching solution (pH=3.5), room temperature for 1 week).
Bi_2Te_3	• Film thickness[9] did not more than 1.5 to 2nm and did not change at room temperature (aging process).
Bi_2Te_3	• Bi $4f_{7/2}$ (157.4 eV) and Bi $4f_{5/2}$ (162.8 eV) contributed[46] to Bi. • Te $3d_{5/2}$ (572.1 eV) and $3d_{3/2}$ (582.6 eV) attributed to Te. Ratio of $d_{5/2}$ to $d_{3/2}$ was 0.69.
ZnTe	• XPS studies confirmed Zn 3p and Te 3d peaks in the obtained samples[67].

Table 5
The XPS data[21] (such as peak positions and the amounts of $NiSe_2/MoSe_2$ composites)

Elements	**Ni 2p**				**Mo 3d**				**Se 3d**	
	0		+2/+3		+4		+6		-2	
	3/2	1/2	3/2	1/2	5/2	3/2	5/2	3/2	3/2	1/2
Peak positions (eV)	853.6	870.9	856.1	873.7	228.4	231.7	232.7	235.5	54.1	55.2
amounts	16.52%		8.77%		14.24%		6.92%		0.49.16%	

All the samples have been synthesized in specific conditions, namely A (cadmium nano particles, 30 nmol deposition), B (selenium nanoparticles, 30 nmol with deposition), C (CdSe nanoparticles, 30 nmol with alternate deposition), D (CdSe nanoparticles, 10 nmol with co-deposition) and E (CdSe thin films, 30 nmol with co-deposition).

The $NiSe_2/MoSe_2$ heterostructures have been produced on graphene nanosheet using hydrothermal reaction[21]. The obtained films could be used as electrocatalyst for hydrogen evolution reaction due to low Tafel slope (65 mV/dec), very small overpotential versus reversible hydrogen electrode (RHE) (144 mV at 10 mA/cm^2) and long-term stability (up to 24 hours). The chemical states of the composites were studied and the XPS results were highlighted in table 5.

The pulsed magnetron sputtering was used to produce films on glass slides[112]. The substrate table could improve adhesion and uniformity (due to heating and rotation). It was noticed that it is very difficult to produce glow discharge if the magnetic field was too small. In contrast, the deposition process will affect the uniformity and utilization rate (target material) if the magnetic field was too large. SEM images confirmed many particles on the film surface and rough morphology. Film thickness was 100 nm. The (211) and (060) planes could be observed in XRD and TEM. In the XPS results (figure 8), peaks at 932.26 eV and 952.16 eV and 934.53 eV and 954.52 eV corresponded to Cu^+ and Cu^{2+} respectively.

The ratio of Cu^+ and Cu^{2+} was 8:1 to 10:1 as indicated in figure 8. The Se 3d consisting of Se $3d_{5/2}$ (54.07 eV) and Se $3d_{3/2}$ (54.95 eV), indicated that selenium existed in Se^{2-} valence. The presence of oxygen (samples' surface have been oxidized) and carbon (carbon added for charging calibration) could be detected in full spectrum analysis. The properties of Ag_2Se, SnSe, MoSSe, ZnSe, Bi_2Se_3, CuSe, $Cu_2ZnSnSe_4$, NiSe, MnZnSe, AgZnSe, PbSe, CdSe, CuSe and Sb_2Se_3 films have been studied using XPS technique. The compositional, phase structure and surface chemistry are reported as in table 6.

XPS studies of metal sulphide films: The growth of zinc sulphide films was seen via chemical bath deposition method[114] using zinc sulfate and thiourea (bath temperature=85 °C, deposition time=120 minutes). XPS analysis (figure 9) revealed that O1s peaks were observed at 531.3 eV to 531.8 eV indicating the presence of $Zn(OH)_2$ (at 530.3 eV), C-O bond (533.3 eV) and ZnO (531.4 eV). It was noted that oxygen existed in the obtained ZnS films (Equation 1 and 2).

In addition, it proved that O1s binding energy (531.8 eV to 531.3 eV) decreased when the Zn/S molar ratio was reduced from 1/50, 1/75,1/100,1/125 to 1/150. All the samples showed absorption edges at 310-320 nm, direct band gap values (3.85 eV to 3.86 eV) and high transmittance value (more than 75%) could be used in buffer layer (solar devices).

$$Zn^{2+} + 2OH^- \rightarrow Zn(OH)_2 \quad (1)$$
$$Zn(OH)_2 \rightarrow ZnO + H_2O \quad (2)$$

The p-type $Cu_2Mg_{0.2}Zn_{0.8}Sn(S,Se)_4$ films have been deposited on soda lime glass through sol-gel spin coating deposition technique (using tin chloride, thiourea, copper acetate, magnesium chloride and zinc acetate) followed by

the selenization treatment[39]. Based on the XRD studies, major (112) peak moved to smaller angles (27.2° to 26.93°) when the annealing temperature was increased from 500 °C to 560 °C, because of variety in atomic lattice distance (elemental replacement process).

In the XPS investigations (figure10), Cu^{+} (Cu $2p_{3/2}$=931.6 eV, Cu $2p_{1/2}$=952.5eV), Zn^{2+} (Zn $2p_{3/2}$=1021.4 eV, Zn $2p_{1/2}$=1044.2eV), Sn^{4+} (Sn $3d_{5/2}$=485.5 eV, Sn $3d_{3/2}$=494.1 eV), Se^{2-} (Se $3d_{3/2}$=53.3 eV, Se $3d_{1/2}$=53.8eV), S^{2-} (S $2p_{3/2}$=160.2eV, S $2p_{1/2}$=161.3 eV) and Mg^{2+} (1303.6 eV) are important. Other electrical, compositional and physical properties have been reported in table 7. These were deterioration of crystal quality, carrier concentration and resistivity value when the selenization temperature was increased.

The growth of SnS_2thin films onto glass slides is via spin coating method[28]. These films showed small grains texture with uniformity, free of contaminants and high optical transmittance value (90%). XPS spectra revealed that the obtained films contained sulphur (S^{2-} ion) and tin (Sn^{4+} ion). The S $2p_{5/2}$ (162.5eV), S $2p_{3/2}$ (161.2eV), Sn $3d_{5/2}$ (486.3 eV) and Sn $3d_{3/2}$ (494.6 eV) could be confirmed in the XPS results. These films could be used as alternative buffer in the solar cell devices (glass/Mo/Cu(In,Ga)Se_2/SnS_2 (50 nm thick)/i-ZnO/AZO/Ag-Ni). Solar cell parameters such as short circuit current density (25.7 mA/cm^2), open circuit voltage (0.41V), fill factor (49%), power conversion efficiency (5.1%), shunt resistance (255 Ωcm^2) and series resistance (13.2 Ωcm^2) were studied.

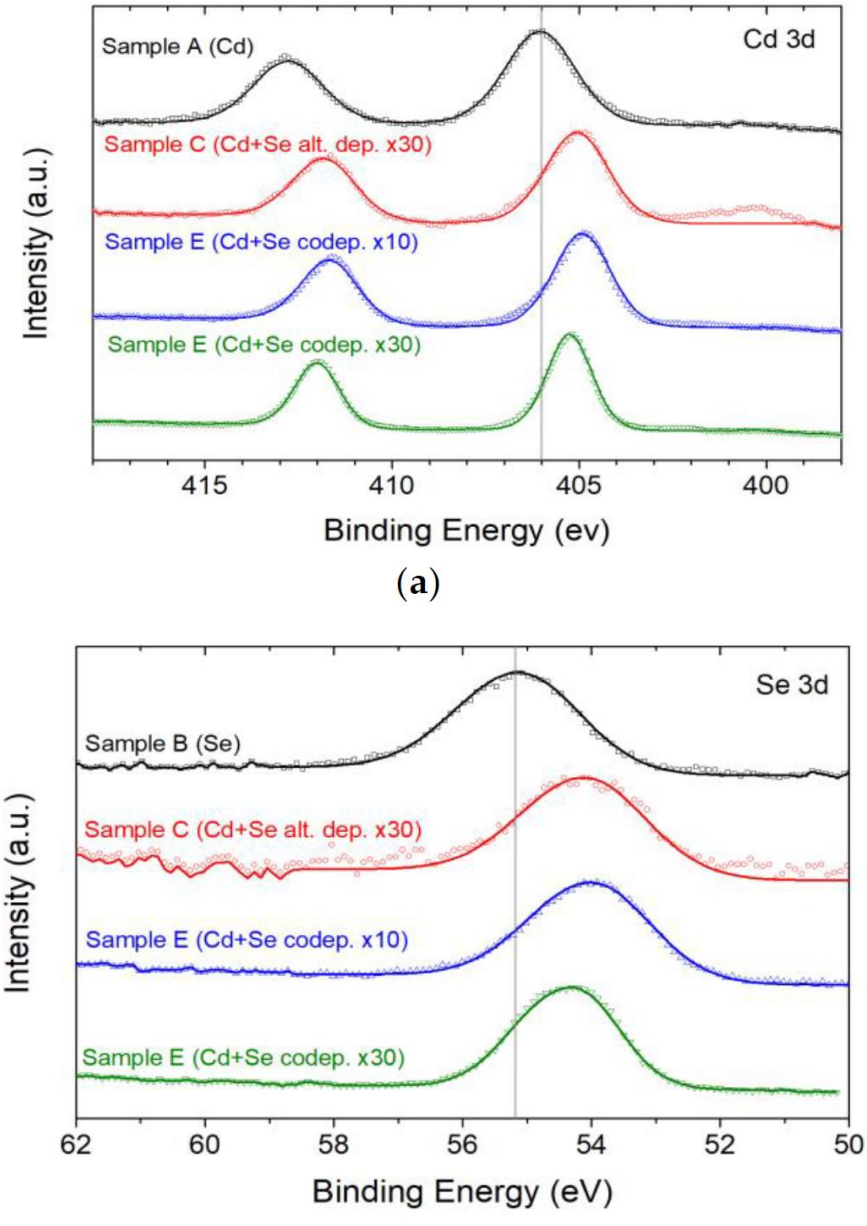

Figure 7: XPS spectra[107] of the prepared samples. (a) Spectra of Cd 3d zone (A, C, D and E). (b) Spectra of the Se 3d zone (B, C, D and E)

Table 6
XPS results for the different types of metal selenide thin films

Thin films	Highlighted XPS results
Ag_2Se	• Ag $3d_{5/2}$ (368 eV), Ag $3d_{3/2}$ (374 eV) indicated Ag^+, while Se $3d_{5/2}$ (53.6 eV), Se $3d_{3/2}$ (54.4 eV) attributed to Se^{2-} for the films[48] prepared in specific conditions (method= SILAR, substrate=stainless steel, temperature=300K, precursor=silver nitrate, Na_2SeSO_3,).
SnSe	• The Sn:Se ratio was 1.7:1 (excess of tin) • Sn 3d5/2 (485.6 eV) and Se 3d5/2 (53.3 eV) peaks could be seen[60].
SnSe	• It indicated slightly tin enrichment (Sn:Se ratio was 1.6:1). • Se $3d_{5/2}$ and Sn $3d_{5/2}$ assigned to 53.5 eV and 485.7 eV, respectively[10].
MoSSe	• XPS analysis revealed that 22% exchange of sulfur by selenium[80].
ZnSe	• XPS results[66] showed the binding energies of Se $3d_{5/2}$ (53.9 eV), Se $3d_{3/2}$ (59.2 eV) and Zn $2p_{3/2}$ (1022 eV).
Bi_2Se_3	• Peak positions at 158.4 eV (Bi $4f_{7/2}$), 163.7 eV (Bi $4f_{5/2}$), 53.8 eV (Se $3d_{5/2}$) and 54.4 eV (Se $3d_{3/2}$) could be observed[11].
CuSe	• Binding energies at 932.31 eV and 53.9 eV, assigned to Cu^{2+} and Se^{2-} in the obtained sample[104].
$Cu_2ZnSnSe_4$	• The concentration of copper (25%), zinc (12.5%), tin (12.5%) and selenium (50%) were measured[110]. • The presence of the oxygen content (1-2%) could be observed after post-deposition process.
CuSe	• The existence of both Se^{2-} (52-56 eV) and Cu^+ content based on the XPS data. • The atomic ratio for copper/selenium (1.8 to 2) was determined[56].
NiSe	• Ni $2p_{3/2}$ and Ni $2p_{1/2}$ peaks could be seen[97] at 852.6 eV and 869.8 eV. • The Se $3d_{5/2}$ peaks at 54.7 eV.
MnZnSe, AgZnSe	• All the Ag (Ag $3d_{5/2}$=367.9 eV, Ag $3d_{3/2}$=374 eV), Zn (Zn $2p_{1/2}$=1021.3 eV, Zn $2p_{3/2}$=1044.5 eV) and Se (Se $3d_{5/2}$=53.8 eV, Se $3d_{3/2}$=54.6 eV) could be detected. • All the Mn (Mn $2p_{3/2}$=641.8eV), Zn (Zn $2p_{1/2}$=1021.4 eV, Zn $2p_{3/2}$=1044.5 eV) and Se (Se $3d_{5/2}$=53.8 eV, Se $3d_{3/2}$=54.6 eV) could be seen[25].
PbSe	• The peaks at 137 eV, 142 eV and 52.96 eV were contributed to Pb $4f_{7/2}$, Pb $4f_{5/2}$ and Se $3d_{5/2}$, respectively[6].
PbSe	• The Pb 4f consisted of 4f5/2 (141.7 eV) and 4f7/2 (136.9 eV). • Binding energies (52-58 eV) correspond[85] to Se 3d.
CdSe	• It was noticed[90] that intensity of Cd-core increased when the Cd/Se ratio was increased (1:1 to 3:1). • It was interesting to note that the highest selenium intensity could be found when the precursor ratio was 2:1.
Bi_2Se_3	• The ratio of atomic concentration of bismuth (Bi) and selenium was 0.7 in the films prepared using thermal evaporation method[83]. • The obtained layer contains selenium oxides.
CuSe	• The Cu 2p contained Cu $2p_{3/2}$ (932.1 eV) and Cu $2p_{1/2}$ (952.2 eV). • The Se 3d consisted[8] of $3d_{5/2}$ (53.8 eV) and $3d_{3/2}$ (54.5 eV).
ZnSe	• In the annealed films, the major peak at 54.2 eV attributed to Se 3d. The intensities of Se^{4+} and Se° were greatly reduced. • Zinc to selenium (Se) ratio was 9:1 in electrodeposited films[51].
SnSe	• The presence of selenium (34.9%), tin (38.8%), oxygen (13.8%) and carbon (12.5%) could be seen in reddish brown films[94]. • Atomic concentration of 47.4% and 43.1% for tin and selenium (after 2 minutes sputtering).
ZnSe	• Several peak positions such as 1045 eV (Zn $2p_{1/2}$), 1022 eV (Zn $2p_{3/2}$), 170 eV (Se $3p_{1/2}$), 165 eV (Se $3p_{3/2}$), 140 eV (Zn 3s), 89 eV (Zn $3p_{3/2}$ or Zn $3p_{1/2}$), 10 eV (Zn 3d) could be observed[72].
Sb_2Se_3	• The presence of Sb (Sb $3p_{3/2}$=766.4 eV, Sb $3d_{5/2}$=529.57 eV) and Se (Se $3d_{5/2}$=54.64 eV, Se $3P_{3/2}$=161.4 eV) binding energy peaks[4] could be observed in the obtained films (precursors=Sodium selenosulphate, antimony (III) chloride, temperature=room temperature, time=1 hour, method=chemical bath deposition, substrate=glass slide).
Sb_2Se_3	• Several peaks[35] included 31.6 eV (Sb $4d_{5/2}$), 32.9 eV (Sb $4d_{3/2}$), 55 eV (Se $3d_{5/2}$) and 55.8 eV (Se $3d_{3/2}$) could be detected.

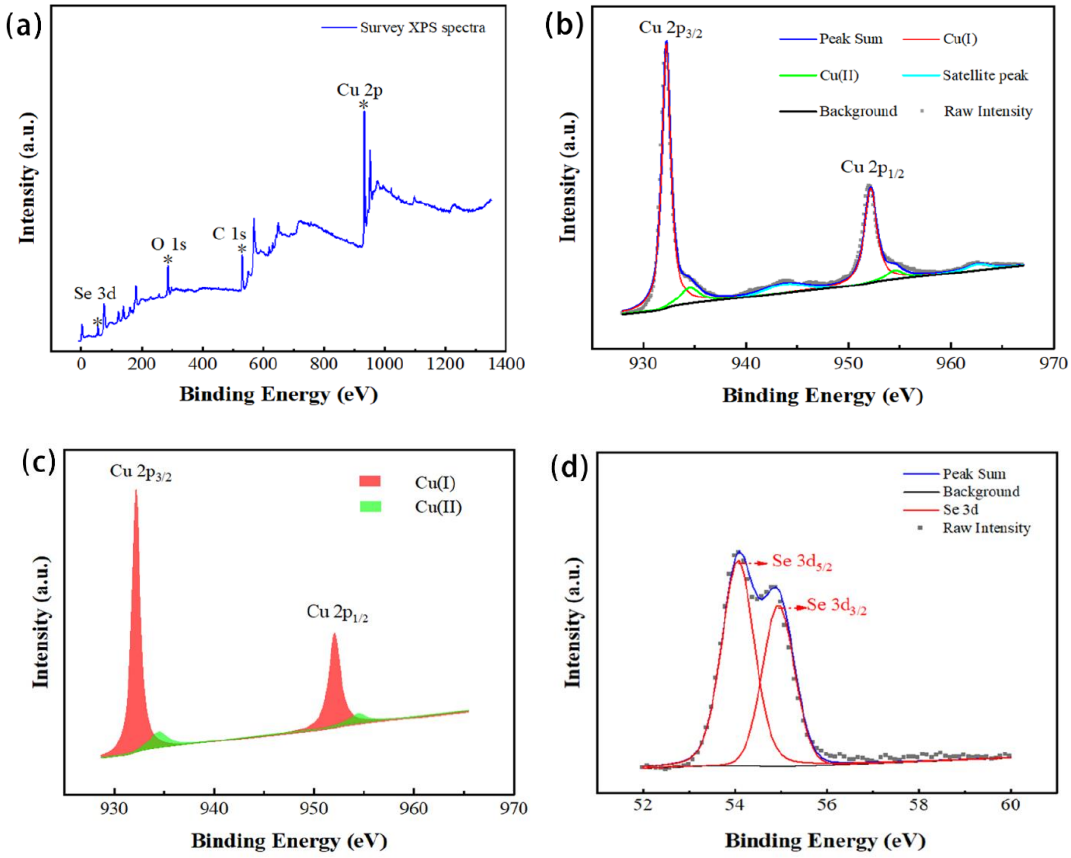

Figure 8: XPS analysis[112] of Cu_2Se films. (a) Survey. (b) Cu 2p. (c) Cu(I):Cu(II). (d) Se 3d.

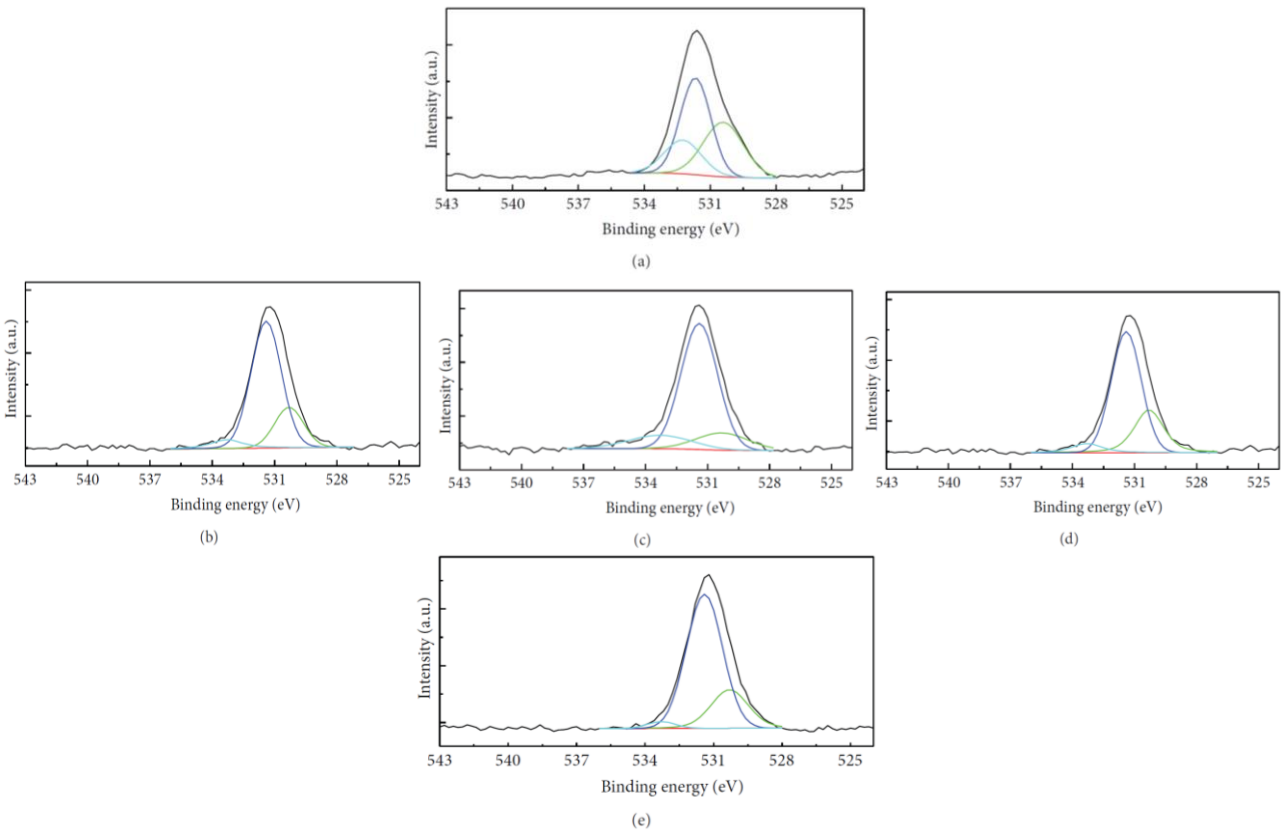

Figure 9: XPS spectra[114] of O1s core level for samples (A=Zn/S molar ratio of 1/50, B= Zn/S molar ratio of 1/75, C= Zn/S molar ratio of 1/100, D= Zn/S molar ratio of 1/125 and E= Zn/S molar ratio of 1/150).

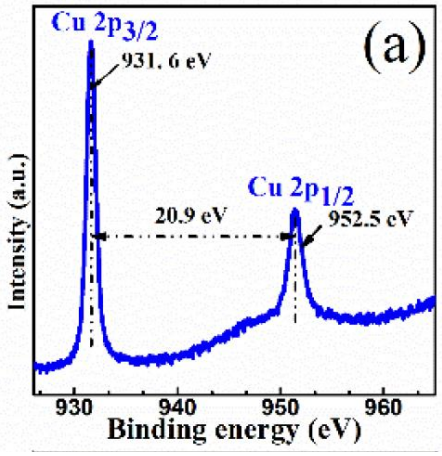
Cu 2p3/2
931. 6 eV
(a)
Cu 2p1/2
20.9 eV
952.5 eV
Intensity (a.u.)
930
940
950
960
Binding energy (eV)

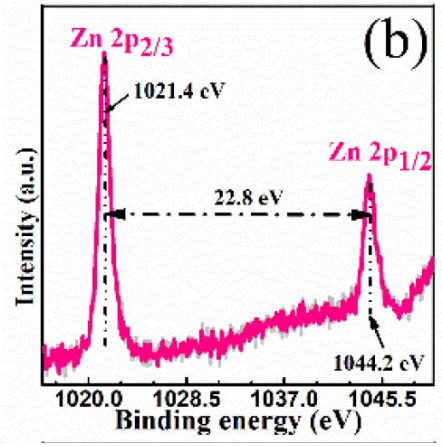
Zn 2p2/3
(b)
1021.4 eV
Zn 2p1/2
22.8 eV
1044.2 eV
Intensity (a.u.)
1020.0
1028.5
1037.0
1045.5
Binding energy (eV)

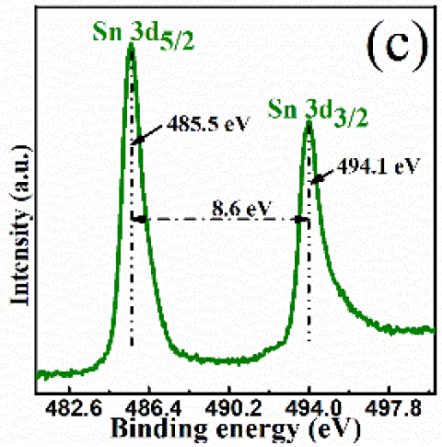
Sn 3d5/2
(c)
485.5 eV
Sn 3d3/2
494.1 eV
8.6 eV
Intensity (a.u.)
482.6
486.4
490.2
494.0
497.8
Binding energy (eV)

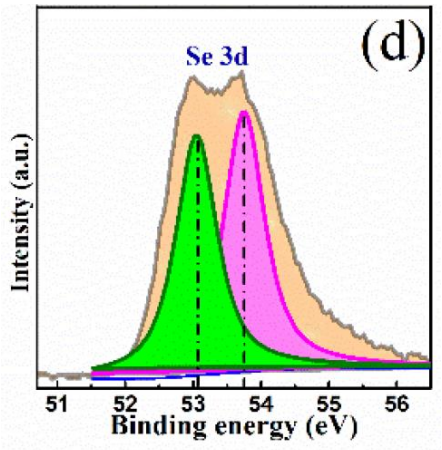
Se 3d
(d)
Intensity (a.u.)
51
52
53
54
55
56
Binding energy (eV)

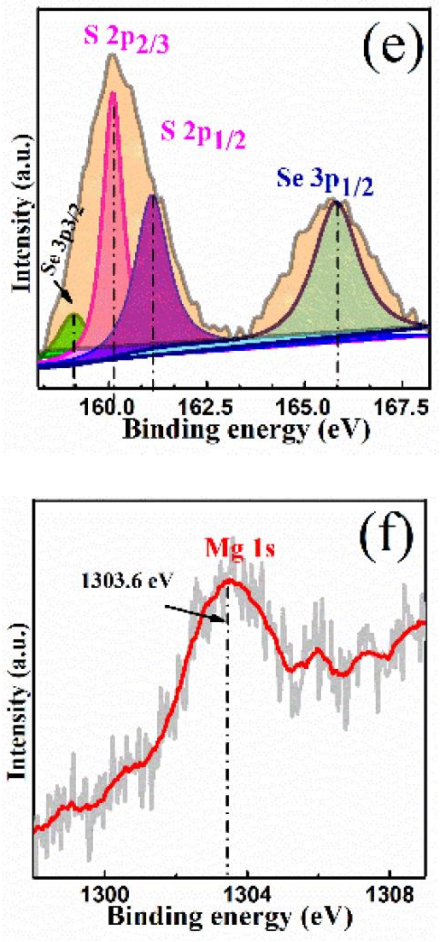

Figure 10: XPS spectra[39] of CMZTSSe thin films annealed for 15 minutes, at annealing temperature of 530 °C.

Table 7
Electrical, compositional and physical properties of the prepared CMZTSSe films[39].

Properties	**Temperature (°C)**		
	500	**530**	**560**
a-axis lattice constant (nm)	0.5669	0.5681	0.5691
c-axis lattice constant (nm)	1.1305	1.1415	1.1635
Crystallite size (nm)	58.2	71.1	67.1
Resistivity (Ω.cm)	$6.18x10^{0}$	$2.85x10^{-1}$	$1.1x10^{2}$
Carrier concentration (cm^{-3})	$9.22x10^{17}$	$6.47x10^{18}$	$5.54x10^{17}$
Mobility ($cm^2/V.s$)	$1.09x10^{0}$	$3.31x10^{-1}$	$1.04x10^{-1}$
Band gap (eV)	1.04	1.02	0.93
Copper (at%)	28.46	26.71	28.32
Zinc (at%)	11.3	9.91	8.16
Tin (at%)	11.14	12.88	13.28
Magnesium (at%)	1.78	1.76	1.88
Sulphur (at%)	11.46	8.67	3.16
Selenium (at%)	35.87	40.08	45.2
Se/(S+Se)	75.79	82.22	93.47
Cu/(Zn+Mg+Sn)	1.18	1.09	1.22
Mg/(Mg+Zn)	0.14	0.15	0.19

Table 8
XPS results for the different types of metal sulfide thin films

Thin films	Highlighted XPS results
$PbS_{0.25}$	• High resolution of Pb 4f (137.59 eV and 142.42 eV) and S 2p (160.76 eV and 162 eV) of the films[105].
$CuFeS_2$	• Thin films[84] were prepared onto glass slides using specific dopant precursor of concentration (0.3 mol) via aerosol-assisted chemical vapour deposition method showed binding energy at 161.3 eV (S $2p_{3/2}$) and 74.65 eV (Cu $3p_{3/2}$).
SnS	• The atomic concentration of 37.5% for sulfur and 40.1% for tin could be observed in as-deposited films[95]. • The atomic concentration of 40.6% for sulfur and 43.2% for tin could be seen in treated films (2+2 minutes sputtering with the argon).
MnS	• The peak at 640.1 eV contributed to Mn $2p_{3/2}$ for the films[69] prepared using 0.5 N sulphuric acid at -100 mV. • The peak at 638.76 eV corresponds to Mn° for the sample produced using 5 N sulphuric acid at -50 mV. • The peak at 640.3 eV contributed to Mn $2p_{1/2}$ for the MnS films prepared using 0.5 N sulphuric acid at +350 mV.
NiS	• Ni $2p_{3/2}$ and S $2p_{3/2}$ could be seen at 853.1 eV and 161.7 eV in millerite phase[23]. • Formation of $NiSO_4$ and $Ni(OH)_2$ were detected for water-reacted surface and air-oxidized surfaces.
Cu_2SnS_3	• S $2p_{3/2}$ and S$2p_{1/2}$ could be represented at 161.2 eV and 162.2 eV, respectively[40]. • Cu $2p_{3/2}$ and Cu $2p_{1/2}$ could be observed at 931.4 eV and 951.2 eV. • Sn $3d_{3/2}$ and Sn $3d_{5/2}$ could be seen at 496 eV and 486 eV.
FeS	• Fe $2p_{3/2}$ and Fe $2p_{1/2}$ were observed[100] at 707 eV and 720 eV. • The intensity of ratio of S $2p_{3/2}$:S $2p_{1/2}$ was 2. • Three major contributions to S 2p could be seen at 162.1eV to 163.3 eV, 162.8 eV to 164 eV and 165 eV to 170 eV.
$CuInS_2$	• The films prepared at 350 °C consisted of 5-8% of oxygen[47]. • Bonding energies were found to be 932.5 eV, 445 eV and 162 eV for Cu $2p_{3/2}$, In $3d_{5/2}$ and S 2p respectively.
CdS, Ag_2S	• Cd $3d_{5/2}$ and Cd 3 $d_{3/2}$ could be represented at 405.4 eV and 412.3 eV, respectively[34]. • There are two sulphur peaks that were detected at 161.5 eV and 168.8 eV in CdS films. • There are two peaks at 368 eV (Ag $3d_{5/2}$) and 161.2 eV (S $2p_{3/2}$) confirmed the formation of Ag_2S films.

The brush electro deposition method[93] has been used to synthesize copper indium gallium selenide (CIGS) thin films (pH=1.5, deposition current density=1 mA/cm^2, substrate=tin oxide coated glass, temperature=80 C, precursors=indium chloride, gallium chloride, SeO_2 and $CuCl_2$). The microstructural parameters such as thickness (500 nm to 1500 nm), grain size (30 nm to 70 nm), strain (0.91 $x10^{-4}$ to 2.51$x10^{-4}$), dislocation density (0.2$x10^{15}$ cm^{-3} to 1.11 $x10^{15}$ cm^{-3}) and lattice parameters (a=0.5623 nm to 0.5765 nm; c=1.1115 nm to 1.1558nm) were reported. In the XPS analysis. Several peaks at 931.9 eV (Cu 2 $p_{3/2}$), 951.2 eV (Cu $2p_{1/2}$), 20 eV (Ga 3d), 54 eV (Se $3d_{3/2}$) could be observed in the $CuIn_{0.5}Ga_{0.5}Se_2$ films at 80 °C.

On the other hand, Cu $2p_{3/2}$ (932.38 eV to 932.216 eV), In $3d_{5/2}$ (441.15 eV to 440.75 eV), In $3d_{3/2}$ (449.15 eV to 448.75 eV) and Ga 3d (19.6 eV to 19.2 eV) moved lower energy, but Se 3d (53.7 eV to 53.8 eV) has shifted to higher energy when the concentration of indium reduced (0.9 to 0.1). Meanwhile, the band gap (1.12 eV to 1.63 eV) and resistivity (0.1 Ω.cm to 12 Ω.cm) increased, but mobility (125 cm^2/V.s to 20.9 cm^2/V.s), carrier density (4.99$x10^{17}$ cm^{-3} to 2.49$x10^{16}$ cm^{-3}) reduced by increasing the concentration of gallium. Thinner samples showed moderate photosensitivity while thicker samples indicated higher photosensitivity value. Experimental results exhibited that recombination centers will reduce photosensitivity.

Electrochemical deposition technique has been used to prepared CZTS films[63] in the specific conditions (substrate=soda lime glass, substrate=copper sulfate, zinc sulphate, tin sulphate, sodium thiosulfate, pH=5, counter electrode=platinum mesh, reference electrode=silver/silver chloride). The 1,8-diiodooctane (DIO) was used as additive to improve crystal structure, increase power conversion efficiency and provide uniformity and smoothness morphology. According to the XPS results, the existence of Cu $2p_{3/2}$ (934.24eV), Cu $2p_{1/2}$ (953.97eV), Zn $2p_{1/2}$ (1025eV), Zn $2p_{3/2}$(1042.29eV), Sn $3d_{3/2}$ (486.52 eV), Sn $3d_{1/2}$ (495.02 eV), S $2p_{3/2}$ (159.91 eV) and S $2p_{1/2}$(165.45eV) could be observed in the sample. Additionally, the XPS data confirmed Cu^+, Zn^{2+}, Sn^{4+} and S^{2-} valence states, perfectly match to stoichiometric of films. It was noted that the band gap values were in the range of 1.51 eV to 1.62 eV and high

absorption coefficient (more than 10^4 cm^{-1}). The open circuit voltage (432 to 456 mV), fill factor (61.3 to 64.3%), short circuit current density (11.74 to 16.44 mA/cm^2), power conversion efficient (2.36 to 4.82%) and shunt resistance (443.2 to 958.6 Ωcm^2) increased, but series resistance reduced (23.37 to 14.27 Ωcm^2) when the concentration of additive was increased from 5 to 20 mg/mL.

The copper sulfide thin films could be used in radio waves (active absorbent), infrared radiation (polarizer), solar cells and photodetectors. These semiconductors have high absorption co-efficient (1.48 x10^4 to 1.52x10^4 cm^{-1}) with indirect band gap (1.25 eV to 1.3 eV). The copper sulfide layers were obtained through sorption-diffusion technique in polyamide matrix[102]. Copper XPS spectra (copper (I) bond observed in deeper layer) and S 2p spectra (sulfide bond seen after cleaning surface with positive argon ion) were reported. According to structural studies, the obtained samples contained Cu_2S (35.6 nm) and $Cu_{1.9375}S$ phase (54.17 nm). The sheet resistance varies from 6300 to 102 Ω/cm^2. The properties of $CuFeS_2$, $PbS_{0.25}$, NiS, Cu_2SnS_3, MnS, FeS, CdS, Ag_2S, $CuInS_2$ and SnS films have been studied using XPS technique. The compositional, phase structure and surface chemistry are reported as in table 8.

Conclusion

X-ray photoelectron spectroscopy is a sensitive electron spectroscopy technique used to determine the quantitative elemental composition and oxidation state of materials, stoichiometry, electrical state and to examine surface contamination. In this work, the advantages and limitations of XPS technique were described. Experimental results showed that the stoichiometric films, compositional and oxidation states were strongly depending on specific experimental conditions.

Acknowledgement

This research work was financially supported by INTI International University (Ho SM).

References

1. Abbas A., West D., Bowers W. and Sampath W., The Effect of Cadmium Chloride Treatment on Close-Spaced Sublimated Cadmium Telluride Thin-Film Solar Cells, *IEEE J. Photovoltaics*, **3**, 1361-1366 **(2013)**

2. Akash H., Sreeram S. and Sundaram B., Effect of annealing temperature on radio frequency sputtered p-type delafossite copper chromium oxide ($CuCrO_2$) thin films and investigation of diode characteristics forming transparent pn-heterojunction, *Coating*, https://doi.org/10.3390/coatings13020263 **(2023)**

3. Anila E., Safeera A. and Reshmi R., Photoluminescence of Nanocrystalline ZnS Thin Film Grown by Sol–Gel Method, *J Fluoresc*., **25**, 227–230 **(2015)**

4. Anu K., Melda F. and Lakshmi M., Effect of selenisation on the properties of antimony selenide thin films, IOP Conf. Ser. Mater. Sci. Eng., doi:10.1088/1757-899X/872/1/012151 **(2020)**

5. Baer R., Kateryna A., Linford R. and Peter M., Practical guides for x-ray photoelectron spectroscopy: First steps in planning, conducting and reporting XPS measurement, *J. Vacuum Sci. Technol. A*, **37**, https://doi.org/10.1116/1.5065501 **(2019)**

6. Bhat T., Devan R., Ma R. and Patil P., Structural and electrochemical analysis of chemically synthesized microcubic architectured lead selenide thin films, *Appl. Phys. A*, https://doi.org/10.1007/s00339-017-1441-0 **(2018)**

7. Bin L., Li B., Lei Z., Feng L., Di X. and Wei L., Preparation and Characterization of Sb_2Te_3 Thin Films by Co-evaporation, *Int. J. Photoenergy*, doi:10.1155/2010/476589 **(2010)**

8. Biswarup C., Driess M., Menezes W. and Viktor H., Crystalline Copper Selenide as a Reliable Non-Noble Electro(pre)catalyst for Overall Water Splitting, *Chem Sus Chem*, **13**, 3222– 3229 **(2020)**

9. Budnik A., Fedorov A., Rogacheva E. and Sipatov A., Growth and structure of thermally evaporated Bi_2Te_3 thin films, *Thin Solid Films*, **612**, 128-134 **(2016)**

10. Burton R., Connor A., Iris N. and Carnie J., Full Thermoelectric Characterization of Stoichiometric Electrodeposited Thin Film Tin Selenide (SnSe), *ACS Appl. Mater. Interfaces*, **12**, 28232-28238 **(2020)**

11. Bushra I. and Chatterjee R., Characterization and synthesis of Bi_2Se_3 topological insulator thin film using thermal evaporation, *Adv. Mater. Lett.*,**7**, 886-890 **(2016)**

12. Celso I., Abramof E., Paulo H. and Thiago R., Incorporation of Europium in Bi_2Te_3 Topological Insulator Epitaxial Films, *J. Phys. Chem. C*, **124**, 16048-16057 **(2020)**

13. Chang C., Lai C., Jiang W., Li Y. and Choi C., Fabrication and Characterization of P-Type Semiconducting Copper Oxide-Based Thin-Film Photoelectrodes for Solar Water Splitting, *Coatings*, https://doi.org/10.3390/ **(2022)**

14. Chao Z., Jim A., Reyes S. and Adriana R., Cadmium telluride (CdTe) and cadmium selenide (CdSe) leaching behavior and surface chemistry in response to pH and O_2, *J. Environ. Manage*., **154**, 78-85 **(2015)**

15. Chen C., Her J. and Pan T., Structural properties of ferroelectric characteristics of mixed $NiTiO_3$-$BiFeO_3$ thin film by the sol-gel method, *J. Phys. Chem. Solids*, https://doi.org/10.1016/ j.jpcs.2021.109986 **(2021)**

16. Chen X., Wang X. and De F., A review on C1s XPS-spectra for some kinds of carbon materials, *Fuller. Nanotub. Carbon Nanostructures*, **28**, 1048-1058 **(2020)**

17. Choi B., Kim H. and Jeon N., Uniformity of HfO_2 Thin Films Prepared on Trench Structures via Plasma-Enhanced Atomic Layer Deposition, *Nanomaterials*, https://doi.org/10.3390/ nano13010161 **(2023)**

18. Conor P., Oliver H., John B., Cansu I. and Georg S., Synthesis and thermal stability of TMD thin films: a comprehensive XPS and Raman study, *Mater. Sci*., https://doi.org/10.48550/ arXiv.2106.07366 **(2021)**

19. Cornette P., Zanna S., Costa D. and Marcus P., The native oxide film on a model aluminium-copper alloy studied by XPS and ToF-SIMS, *Corros. Sci.*, https://doi.org/10.1016/j.corsci.2020.108837 **(2020)**

20. Cuello N., Monica E., Oliva M. and Elias V., Development of iron modified MCM-41 as promising nano-composites with specific magnetic behavior, *Microporous Mesoporous Mater.*, **203**, 106-115 **(2015)**

21. Dai T., Zhou Z., Han X., Wang X. and Luo Y., *In Situ* Growth of $NiSe_2$-$MoSe_2$ Heterostructures on Graphene Nanosheets as High-Performance Electrocatalyst for Hydrogen Evolution Reaction, *Catalysts*, https://doi.org/10.3390/catal12070701 **(2022)**

22. Dale L., Ma Z., Olson A. and Topp E., Molecular Characterization of Gadolinium-Doped Zinc telluride films by x-ray photoelectron spectroscopy, *J. Spectroscopy*, **30**, 38-43 **(2015)**

23. Daniel L., Wayne N. and Bancroft M., X-ray photoelectron spectroscopic study of a pristine millerite (NiS) surface and the effect of air and water oxidation, *Am. Min*., **83**, 1256–1265 **(1998)**

24. Domashevskaya E. et al, XPS and XANES studies of SnOx nanolayers, *J. Struct. Chem*., **49**, S80-S91 **(2008)**

25. Fen Q., Liang Q., Bian J. and Hou X., Tunability in the Optical and Electronic Properties of ZnSe Microspheres via Ag and Mn Doping, *ACS Omega*, **4**, 12271-12277 **(2019)**

26. Fondell M., Gorgoi M., Boman M. and Lindblad A., Surface modification of iron oxides by ion bombardment – Comparing depth profiling by HAXPES and Ar ion sputtering, *J. Electron Spectros. Relat. Phenomena*, **224**, 23-26 **(2018)**

27. Garcia J., Pal U. and Galindo G., Au–Al_2O_3 nanocomposites: XPS and FTIR spectroscopic studies, *Sol. Energy Mater. Sol. Cells*, **82**, 291-298 **(2004)**

28. Gedi S., Alhammadi S., Noh J. and Minnam R., SnS_2 Nanoparticles and Thin Film for Application as an Adsorbent and Photovoltaic Buffer, *Nanomaterials*, https://doi.org/10.3390/nano12020282 **(2022)**

29. Guzelcimen F., Merve S., Unlu M. and Baris K., The effect of thickness on surface structure of rf sputtered TiO_2 thin films by XPS, SEM/EDS, AFM and SAM, *Vacuum*, https://doi.org/10.1016/j.vacuum.2020.109766 **(2020)**

30. Hirpara A., Chaki S. and Kannaujiya R., Photoresponse application of the dip-coated Cu_2ZnSnS_4 thin film, *Appl. Phys. A*., https://doi.org/10.1007/s00339-023-06507-2 **(2023)**

31. Ho S.M., A brief review of the growth of pulsed laser deposited thin films, *Br. J. Appl. Sci. Technol.*, **14**, 1-6 **(2016)**

32. Ho S.M., Studies of Power Conversion Efficiency and Optical Properties of $Ni_3Pb_2S_2$ Thin Films, *Makara J. Sci.*, **21**, 119-124 **(2017)**

33. Ho S.M., An investigation of SILAR grown cobalt selenide thin films, *Asian J. Basic Sci. Res*., **4**, 1-9 **(2022)**

34. Hota G., Idage S. and Kartic C., Characterization of nano-sized CdS-Ag_2S Core-Shell Nanoparticles Using XPS Technique, *Colloids Surf. A Physicochem. Eng. Asp*., **293**, 5-12 **(2007)**

35. Huw S., Oliver S., Tim D., Major D. and Ken D., Chemical etching of Sb2Se3 solar cells: surface chemistry and back contact behaviour, *J. Phys. Energy*, https://doi.org/10.1088/2515-7655/ab3c98 **(2019)**

36. Ingrida A., Skirma Z. and Vitalijus J., X-ray photoelectron spectroscopy investigation of CuxS–CuyTe layers on polyamide film formed by the use of potassium telluropentathionate, *Chemija*, **20**, 162-168 **(2009)**

37. Isaacs A., Lee R., David M. and Josh D., Advanced XPS characterization: XPS-based multi-technique analyses for comprehensive understanding of functional materials, *Mater. Chem. Front*., **5**, 7931-7963 **(2021)**

38. Jacob A., Abdul W. and Mailin M., Operational Stability, Regenerability and Thermodynamics Studies on Biogenic Silica/Magnetite/Graphene Oxide Nanocomposite-Activated Candida rugosa Lipase, *Polymers*, https://doi.org/10.3390/polym13213854 **(2021)**

39. Jiang D., Wang F., Yao B., Wang Z. and Yang L., Investigation on the Selenization Treatment of Kesterite $Cu_2Mg_{0.2}Zn_{0.8}Sn(S,Se)_4$ Films for Solar Cell, *Nanomaterials*, **9**, doi:10.3390/nano9070946 **(2019)**

40. Jianmin L., Liu W., Zhu C., Yan Z. and Huang J., Solution-processed Cu_2SnS_3 thin film solar cells, *RSC Adv*., DOI: 10.1039/c6ra09389b **(2016)**

41. Jothibas M., Johnson J. and Manoharan C., Structural and optical properties of zinc sulphide nanoparticles synthesized via solid state reaction method, *J. Mater. Sci. Mater. Electron*., **28**, 1889–1894 **(2017)**

42. Julian M., Galia P., Cruz M. and Alvaro C., Nanostructured Lead Dioxide Thin Electrode, *Electrochem. Solid-State Lett.*, **7**, A75-A77 **(2004)**

43. Jungjoon P., Seo J., Lim J. and Yoo B., Synthesis of Copper Telluride Thin Films by Electrodeposition and Their Electrical and Thermoelectric Properties, *Front. Chem*., doi: 10.3389/fchem.2022.799305 **(2022)**

44. Kang J., Vinod K., Lee H. and Mark C., Solution-Processed Layered Gallium Telluride Thin-Film Photodetectors, *ACS Photonics*, DOI: 10.1021/acsphotonics.8b01066 **(2018)**

45. Kaspar P., Dinara S., Alois N. and Sahar R., Characterization of Fe_2O_3 thin film on highly oriented pyrolytic graphite by AFM, Ellipsometry and XPS, *Appl. Surf. Sci*., **493**, 673-678 **(2019)**

46. Katarina C., Andrew L., Reid G., Meng L. and Kees H., Thermoelectric Properties of Bismuth Telluride Thin Films Electrodeposited from a Nonaqueous Solution, *ACS Omega*, **5**, 14679-14688 **(2020)**

47. Katerski A., Mere A. and Krunks M., Effect of the growth temperature on chemical composition of spray deposited $CuInS_2$ thin films, *Energy Proc*., **2**, 103–107 **(2010)**

48. Kedara T., Sankapal R. and Kumar B., Pseudocapacitive nanostructured silver selenide thin film through room temperature chemical Route: First approach towards supercapacitive

application, *Inorg. Chem. Commun*., https://doi.org/10.1016/j.inoche.2021.109083 **(2022)**

49. Khan I., Idrees K. and Khalid S., Nanoparticles: properties, applications and toxicities, *Arab. J. Chem*., **12**, 908-931 **(2019)**

50. Kim J., Le T., Ahn B. and Seo H., Pre-oxidation effects on properties of bismuth telluride thermoelectric composites compacted by spark plasma sintering, *J. Asian Ceram. Soc*., **8**, 211-221 **(2020)**

51. Klochko N., Volkova N., Kopach V. and Karasyov S., Influence of vacuum annealing on the composition of electro chemically deposited zinc selenide layers, *Funct. Mater.*, **12**, 35-40 **(2005)**

52. Kogo G., Lee H., Adem H., Bo X. and Sangram K., Highly-efficient thermoelectric pn-junction device based on bismuth telluride (Bi_2Te_3) and molybdenum disulfide (MoS_2) thin films fabricated by RF magnetron sputtering technique, *J. Appl. Phys*., https://doi.org/10.1063/1.5046686 **(2018)**

53. Krishna D. and Philip J., Review on surface-characterization applications of X-ray photoelectron spectroscopy (XPS): Recent developments and challenges, *Appl. Surf. Sci. Adv*., https://doi.org/10.1016/j.apsadv.2022.100332 **(2022)**

54. Lederer S., Han J. and Schreiber S., XPS studies of Cs_2Te photocathodes, Proceedings of FEL 2007, Novosibirsk, Russia, 457-460 **(2007)**

55. Lefebvre J., Galli F., Claudia B. and Daria C., Experimental methods in chemical engineering: X-ray photoelectron spectroscopy-XPS, *Can. J. Chem. Eng*., **97**, 2588-2593 **(2019)**

56. Lin Z., Hollar C., Hu Y., Zhang Y. and Yin A., A Solution Processable High-Performance Thermoelectric Copper Selenide Thin Film, *Adv. Mater*., https://doi.org/10.1002/adma.201606662 **(2017)**

57. Maksimov S., Smirnov A., Rumyantseva M. and Krivetskiy V., Electrical and Gas Sensor Properties of Nb(V) Doped Nanocrystalline-Ga_2O_3, *Materials*, https://doi.org/10.3390/ **(2022)**

58. Mane M. et al, Synthesis and X-ray photoelectron spectroscopy (XPS) and thermoelectric studies of ternary $Bi_2(Te_{0.5}Se_{0.5})_3$ mixed-metal chalcogenide thin films by the arrested precipitation technique, *Can. J. Chem*., **89**, 1375–1381 **(2011)**

59. Maslakov I., Yury A., Popel A. and Ian F., XPS study of ion irradiated and unirradiated CeO_2 bulk and thin film samples, *Appl. Surf. Sci*., **448**, 154-162 **(2018)**

60. Matthew R., Liu T., Adam P., Carnie M. and Jenny B., Thin Film Tin Selenide (SnSe) Thermoelectric Generators Exhibiting Ultralow Thermal Conductivity, *Adv. Mater*., DOI: 10.1002/adma.201801357 **(2018)**

61. Maximov M., Yury K., Oleg M. and Ezhov I., Atomic Layer Deposition of Lithium–Nickel–Silicon Oxide Cathode Material for Thin-Film Lithium-Ion Batteries, *Energies*, https://doi.org/10.3390/en13092345 **(2020)**

62. Mehdi S., Raya E., Ajili L. and Najoua K., Physical properties evolution of sprayed Cu_2MgSnS_4 thin films with growth parameters and vacuum annealing, *Superlattices Microstruct*, https://doi.org/10.1016/j.spmi.2020.106711 **(2020)**

63. Mkawi E., Al-Hadeethi Y., Arkook B. and Bekyarova E., Impact of 1,8-Diiodooctane (DIO) Additive on the Active Layer Properties of Cu_2ZnSnS_4 Kesterite Thin Films Prepared by Electrochemical Deposition for Photovoltaic Applications, *Materials*, https://doi.org/10.3390/ma16041659 **(2023)**

64. Mohamad N., Nur H., Nor A. and Huyop F., An overview of technologies for immobilization of enzymes and surface analysis techniques for immobilized enzymes, *Biotechnol. Biotechnol. Equip*., **29**, 205-220 **(2015)**

65. Morazzoni F., Canevali C., Armelao L. and Depero L., Surface reactivity of nanostructured tin oxide and Pt-doped tin oxide as studied by EPR and XPS spectroscopies, *Mater. Sci. Eng. C*, **15**, 167–169 **(2001)**

66. Murali R., Ooomen R. and Vasantha S., Properties of ZnSe films pulse plated on high temperature substrates, *Chalcogen. Lett*., **5**, 111–116 **(2008)**

67. Murali R., Ziaudeen M. and Jayaprakash N., Structural and electrical properties of brush plated ZnTe films, *Solid State Electron*., **50**, 1692–1695 **(2006)**

68. Murthy M., Sreelatha C., Ravinder G. and Anusha S., The effect of solution pH on the structural, surface morphological and optical characteristics of ZnO thin films synthesized by the chemical bath deposition technique, *Mater. Today Proc*., **54**, 602-607 **(2022)**

69. Natarajan R., Palaniswamy N., Natesan M. and Muralidharan V., XPS Analysis of Passive Film on Stainless Steel, *Open Corros. J*., **2**, 114-124 **(2009)**

70. Nazar S., Waqar M., Nadeem N. and Zeb A., The synthesis of CdZnTe semiconductor thin films for tandem solar cells, *RSC Adv*., **11**, 39940-39949 **(2021)**

71. Neudachina V., Tamm M., Yashina L. and Shtanov V., XPS study of SnTe(100) oxidation by molecular oxygen, *Surf. Sci*., **584**, 77-82 **(2005)**

72. Noble A. and Ralph G., Assembly and Characterization of SAMs Formed by the Adsorption of Alkanethiols on Zinc Selenide Substrates, *Langmuir*, **17**, 3937-3944 **(2001)**

73. Noraini K., Anuar K., Ho S.M. and Saravanan N., XRD and AFM studies of ZnS thin films produced by electro deposition method, *Arab. J. Chem*., **3**, 243-249 **(2010)**

74. Okal J., Tylus W. and Kepinski L., XPS study of oxidation of rhenium metal on γ -Al_2O_3 support, *J. Catal*., **225**, 498–509 **(2004)**

75. Oswald S., Lattner E., Menzel S. and Seifert M., AES and XPS depth-profiling of annealed AlN/Ti-Al/AlN films for high-temperature applications in SAW metallization, *Surf. Interface Anal*., **50**, 991-995 **(2018)**

76. Pandian S., Adnan J., Najwa M. and Siti N., The preparation and application of zinc sulfide as photocatalyst for water remediation: A mini review, *Malaysian J. Anal. Sci*., **26**, 318–333 **(2022)**

77. Parashurama S., Ali M. and Kekuda D., Investigation on tailoring physical properties of Nickel Oxide thin films grown by dc magnetron sputtering, *Mater. Res. Express*, DOI:10.1088/2053-1591/ab69c5 **(2020)**

79. Peng W., Wuu S., He J., Ou S. and Horng R., Tunability of p- and n-channel TiOx thin film transistors, *Sci. Rep.*, DOI:10.1038/s41598-018-27598-5 **(2018)**

79. Petrova D., Napoleonov B., Minh C. and Marinova V., The Effect of Post Deposition Treatment on Properties of ALD Al-Doped ZnO Films, *Nanomaterials*, https://doi.org/10.3390/nano13050800 **(2023)**

80. Quan M., Chen S., Klee V., Sarah B., Le D. and Greg P., Postgrowth Tuning of the Bandgap of single layer molybdenum disulfide films by sulfur/selenium exchange, *ACS Nano*, **8**, 4672-4677 **(2014)**

81. Ranganaik V., Harish N., Mustur C. and Kumar Y., Studies on Characterization, Optical Absorption and Photoluminescence of Yttrium Doped ZnS Nanoparticles, *J. Nanotechnol*., https://doi.org/10.1155/2014/924797 **(2014)**

82. Rath S., Sarangi N., Varma S. and Sahu N., Surface characterization and electronic structure of HgTe nanocrystalline thin films, *Phys. Rev. B.*, https://link.aps.org/doi/10.1103/PhysRevB.72.205410 **(2005)**

83. Rogacheva E., Sipatov A., Fedorov A. and Mateychenko P., Structural of thermally evaporated bismuth selenide thin films, *Funct. Mater*., **25**, 516-524 **(2018)**

84. Sadia K., Malik A., Khan Y., Ejaz A. and Paul O., Transition metal doped pyrite (FeS_2) thin films: structural properties and evaluation of optical band gap energies, *J. Mater. Chem. C*., DOI: 10.1039/c5tc03275j **(2015)**

85. Sameer S., Sarma D., Nanda J. and Jennifer A., Unraveling Internal Structures of Highly Luminescent PbSe Nanocrystallites Using Variable-Energy Synchrotron Radiation Photoelectron Spectroscopy, *J. Phys. Chem. B,* **110**, 15244-15250 **(2006)**

86. Santoni A., Alberto M., Matteo V. and Claudia M., Electronic structure of Ar^+ ion-sputtered thin-film MoS_2: A XPS and IPES study, *Appl. Surf. Sci*., **392**, 795-800 **(2017)**

87. Saravanan N., Anuar K., Ho S.M. and Abdul H., Effect of deposition time on surface topography of chemical bath deposited PbSe thin films observed by atomic force microscopy, *Pac. J. Sci. Technol.*, **11**, 399-403 **(2010)**

88. Sellin P., Baker A. and Babar S., An XPS Study of Bromine in Methanol Etching and Hydrogen Peroxide Passivation Treatments for Cadmium Zinc Telluride Radiation Detectors, *Appl. Surf. Sci*., **264**, 681-686 **(2013)**

89. Shangguan H., Li X., Jie S. and Deng Q., Synthesis of lutein esters using a novel biocatalyst of *Candida antarctica* lipase B covalently immobilized on functionalized graphitic carbon nitride nanosheets, *RSC Adv*., **10**, 8949-8957 **(2020)**

90. Sharma S., Himani S. and Singh G., Low energy ion induced effects on TOPO capped CdSe nanocrystals probed by XPS depth profiling and optical measurements, *Nucl. Instrum. Methods Phys. Res. B*., **244**, 86–90 **(2006)**

91. Shtanov V., Yashina V., Kobeleva S. and Shatalova T., XPS study of fresh and oxidized GeTe and žGe,Sn/ Te surface, *Solid State Ion*, DOI: 10.1016/S0167-2738(01)00785-8 **(2001)**

92. Stevie F. and Donley C., Introduction to x-ray photoelectron spectroscopy, *J. Vacuum Sci. Technol. A*, https://doi.org/10.1116/6.0000412 **(2020)**

93. Subiramaniyam P., Thirunavukkarasu P. and Murali K., Photoconductive Properties of Brush Plated Copper Indium Gallium Selenide Films, *J. Coatings*, http://dx.doi.org/10.1155/2013/109176 **(2013)**

94. Subramaniam B., Mary J. and Sanjeeviraja C., Electrodeposition of Sn, Se, SnSe and the material properties of SnSe films, *Thin Solid Films*, **357**, 119-124 **(1999)**

95. Subramanian B., Sanjeeviraja C. and Jayachandran M., Cathodic electrodeposition and analysis of SnS films for photoelectrochemical cells, *Mater. Chem. Phys.*, **71**, 40–46 **(2001)**

96. Sung M., Kim J., Heo T., Park S. and Jae K., The Effect of the Dehydration of MgO Films on their XPS Spectra and Electrical Properties, *J. Electrochem. Soc*., **154**, J408-J412 **(2007)**

97. Swesi A., Masud J. and Nath M., Nickel Selenide As High-efficiency Catalyst for Oxygen Evolution Reaction, *Energy Environ. Sci*., **9**, 1771-1782 **(2016)**

98. Tanmoy P., Movva H., Roy A., Dey R. and Rai A., Angular dependence of magnetization reversal in epitaxial chromium telluride thin films with perpendicular magnetic anisotropy, *J. Magn. Magn. Mater.*, **437**, 72-77 **(2017)**

99. Tanori O., Landin R. and Acosta C., Copper selenide and copper telluride composites powders sintetized by ionic exchange, *Chalcogen. Lett*., **11**, 13–19 **(2014)**

100. Thanh K., Kim H., Park C., Pham T. and Tam T., Effect of sulfur annealing on the morphological, structural, optical and electrical properties of iron pyrite thin films formed from FeS_2 nano-powder, *Korean J. Chem. Eng*, DOI: 10.1007/s11814-018-0060-6 **(2018)**

101. Valeriy K., Sergey M., Andrei S. and Andreev M., Electrical and gas sensor properties of Nb(V) doped nanocrystalline β-Ga_2O_3, *Materials*, https://doi.org/10.3390/ma15248916 **(2022)**

102. Valentina K. and Mindaugas A., Optical, XPS and XRD Studies of Semiconducting Copper Sulfide Layers on a Polyamide Film, *Int. J. Photoenergy*, doi:10.1155/2009/304308 **(2009)**

103. Velusamy P., Babu R., Dahlem M. and Elangovan E., Highly transparent conducting cerium incorporated CdO thin films deposited by a spray pyrolytic technique, *RSC Adv*., DOI: 10.1039/c5ra15262c **(2015)**

104. Vinod P., Kim J. and Jin X., Hexagonal nanoplatelets of CuSe synthesized through facile solution phase reaction, *Mater. Res. Bull*., **46**, 340-344 **(2011)**

105. Vishal V., Devan R., Pawar A., Namdev S. and Ma Y., Chemically synthesized PbS nanoparticulate thin films fora rapid NO_2 gas sensor, *Mater. Sci. Poland*, DOI: 10.1515/msp-2016-0001 **(2016)**

106. Volkova D., Klochko P., Li T. and Kopach V., Electrochemical deposition of cadmium telluride films, *Funct. Mater*., **15**, 119-126 **(2008)**

107. Walter G., Vizza M., Nicola C. and Maria J., Electrodeposition of Nanoparticles and Continuous Film of CdSe on n-Si (100), *Nanomaterials*, doi:10.3390/nano9101504 **(2019)**

108. Waqar M., Nasir M., Bushra P., Nazar A. and Din U., Pronounced Impact of p-Type Carriers and Reduction of Bandgap in Semiconducting ZnTe Thin Films by Cu Doping for Intermediate Buffer Layer in Heterojunction Solar Cells, *Materials*, doi:10.3390/ma12081359 **(2019)**

109. Winiarski J., Tylus W., Irena S. and Bogdan S., XPS and FT-IR Characterization of Selected Synthetic Corrosion Products of Zinc Expected in Neutral Environment Containing Chloride Ions, *J. Spectroscopy*, https://doi.org/10.1155/2018/2079278 **(2018)**

110. Xerxes K., Garris R., Li J. and Teeter G., Co-solvent Enhanced Zinc Oxysulfide Buffer Layers in Kesterite Copper Zinc Tin Selenide Solar Cells, *Phys. Chem. Chem. Phys.*,**17**, 15355-15364 **(2015)**

111. Yaashina L., Kobeleva S., Shatalova B. and Neudachina S., XPS study of fresh and oxidized (Pb,Ge)Te surfaces, *Surf. Interface Anal*., **34**, 498–501 **(2002)**

112. Yang L., Wei J., Qin Y., Wei L. and Song P., Thermoelectric Properties of Cu_2Se Nano-Thin Film by Magnetron Sputtering, *Materials*, DOI: 10.3390/ma14082075 **(2021)**

113. Yazid R., Ho S.M., Tan W.T. and Anuar K., Preparation and characterization of chemical bath deposited NiSe thin films, *Ozean J. Appl. Sci*., **4**, 363-372 **(2011).**

114. Yu F., Ou S., Yao P., Wu B. and Wuu D., Structural, Surface Morphology and Optical Properties of ZnS Films by Chemical Bath Deposition at Various Zn/S Molar Ratios, *J. Nanomaterials*, http://dx.doi.org/10.1155/2014/594952 **(2014)**

115. Yuki N. and Masaya I., Electrochemical Deposition of CuxSnySzO Thin Films and Their Application for Heterojunction Solar Cells, *Int. J. Photoenergy*, doi:10.1155/2012/171432 **(2012)**

116. Zhang Y., Wang Z., Feng J., Ming S., Xia Y. and Qu F., Synthesis and electromagnetic transport of large-area 2D WTe_2 thin film, *J. Semicond*, doi: 10.1088/1674-4926/43/10/102002 **(2022)**.

(Received 08th March 2023, accepted 10th May 2023)

*****